TiO$_2$ Sensitization with Bi$_2$S$_3$ Quantum Dots: The Inconvenience of Sodium Ions in the Deposition Procedure

Inti Zumeta-Dubé,[†] Víctor-Fabián Ruiz-Ruiz,[†] David Díaz,[*,†] Sandra Rodil-Posadas,[‡] and Andreas Zeinert[§]

[†]Facultad de Química, [‡]Instituto de Investigación en Materiales, Universidad Nacional Autónoma de México, Avenida Universidad 3000, Ciudad Universitaria, Coyoacán, CP 04510, México D. F, México

[§]Laboratoire de Physique de la Matière Condensée, Université de Picardie Jules Verne, 33, rue Saint Leu, 80039 AMIENS Cedex 1, France

Ⓢ Supporting Information

ABSTRACT: This paper highlights the inconvenience of sodium ions in the Bi$_2$S$_3$ quantum dots (QDs) deposition procedure, on the TiO$_2$ surface, for the conversion efficiency of the sensitized solar cells derived from these materials. Porous TiO$_2$ electrodes were sensitized with QDs obtained by the successive ion layer adsorption and reaction (SILAR) technique, using aqueous solutions of Bi(NO$_3$)$_3$ as the cation precursor and Na$_2$S as the sulfide source. Independently, elemental sulfur vapor was used to replace the Na$_2$S solution in the synthesis procedure. The obtained layers were characterized by X-ray diffraction, transmission electron microscopy, Raman scattering, and diffuse reflectance spectroscopy. We found that the presence of sodium ions in the reaction system strongly affects the formation of Bi$_2$S$_3$ on the porous TiO$_2$. This result contrasts with what other authors have claimed. Using elemental sulfur vapor as a precursor, crystalline Bi$_2$S$_3$ nanoparticles are formed on the TiO$_2$ surface. The sensitized solar cells produced using the two different types of photoelectrodes were compared based on the photocurrent–voltage characteristic and the photocurrent time stability. The sensitized photoelectrodes derived from elemental sulfur vapor are much more stable over time and can achieve an efficiency of 0.84%. This is the highest conversion efficiency value for any Bi$_2$S$_3$ photoelectrochemical cell.
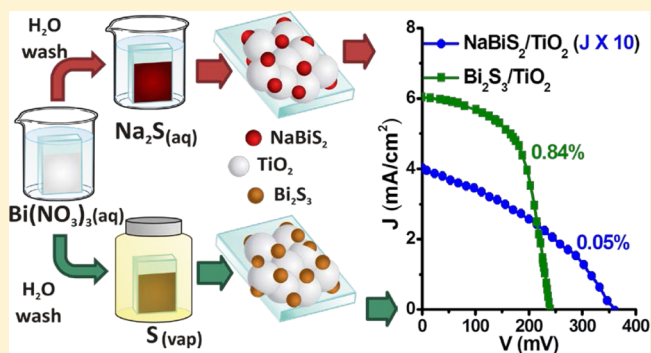
INTRODUCTION

Bismuth sulfide is a material with ideal optical and electric characteristics for many thermoelectric[1] and optoelectronic applications,[2−4] including solar cells.[5] The band gap energy of bulk Bi$_2$S$_3$ is 1.3 eV,[1,6,7] although there are some discrepancies between the values reported in the literature;[7−9] this gap is very close to the optimal Shockley−Queisser value for p−n homojunction solar cells.[10] Also, this material has a large absorption coefficient.[11] These properties are very attractive for photovoltaic conversion. Another interesting issue of this material is that it can be synthesized by easy, low energy consuming and cost-effective methods, which is favorable for its scalable capability. Additionally, Bi$_2$S$_3$ is much less toxic than other optoelectronic materials based on Pb, Cd, or Hg metal cations, or anions such as Te, Se, and As. The materials toxicity could limit, in some way, the achievement of extensive application due to environmental and related regulatory concerns.[2]

Among the most studied types of Bi$_2$S$_3$ solar cells, there are the thin film based devices,[12−14] but to a greater extent, the regenerative photoelectrochemical ones.[15−19] These photovoltaic devices have a relatively low efficiency, typically, less than 0.5%. The reports on types of Bi$_2$S$_3$ solar cells do not explore the size effect of this material on the response as a light harvester. Nanostructured semiconductors have shown very promising perspectives in solar cell applications, not only for the unique properties of low dimensional materials but also due to their low-cost, solution-processability, and scalable potential.[20−22] Recently, notable progress in nanostructured based photovoltaic devices has been reported: (a) Quantum dot sensitized solar cells (QDSSC), using liquid electrolytes, have attained an efficiency record of 6.76%.[23] (b) In solid-state colloidal quantum dot (QD) solar cells, a record of 8.5% has been reached.[24] (c) InP nanowires array solar cells achieved a high 13.8% efficiency.[25] Concerning Bi$_2$S$_3$ nanostructures, Konstantatos et al. reported a 1.6% efficiency in a solid-state p−n junction solar cell formed between p-type PbS colloidal QDs and n-type Bi$_2$S$_3$ nanocrystals.[26]

On the other hand, Bi$_2$S$_3$ has continuously been claimed as a material that has received considerable attention as an absorber

in QDSSC.[27−35] However, only five works[36−40] addressing Bi$_2$S$_3$-QDSSC have been published to date. The reported efficiencies are very low compared with other QDs sensitizers that can range 5−7% in the best devices.[41−44] Vogel et al.[36] sensitized porous TiO$_2$ layers with QDs deposited using the successive ions adsorption and reaction (SILAR) technique. They used one SILAR process and the starting precursors were a saturated solution of Bi(NO$_3$)$_3$ and a 0.5 M solution of Na$_2$S, both in water. The immersion time in each solution was 1 min. The obtained sensitized photoelectrodes could not be deeply studied as they decompose under illumination within minutes.[36] Suárez et al.[37] sensitized SnO$_2$ photoelectrodes applying five SILAR processes of 0.1 M BiI$_3$ and 0.1 M Na$_2$S aqueous solutions. These authors[36,37] reported photoelectrode stability under irradiation with low intensity monochromatic light of 425 nm (1 mW/cm^2). In these two works,[36,37] it was assumed that Bi$_2$S$_3$ was deposited after dipping the Bi(III)-impregnated oxide layers into the Na$_2$S solution, but no further experimental evidence was presented. This assumption contrasts with some experimental evidence presented in this work; we will discuss this aspect below. In a very recent work, Lin and Lee[45] reported the sensitization of SnO$_2$ porous layers with Bi$_2$S$_3$ QDs, by the SILAR technique, starting from 0.01 M Bi(NO$_3$)$_3$ and 0.01 M Na$_2$S solutions in acetone. However, their synthesis results could not be reproduced; for more details on this point and other three works using Bi$_2$S$_3$ as sensitizer, see the Supporting Information. The aforementioned progress and critical views and the small number of related papers in the literature make it imperative to intensify the research on Bi$_2$S$_3$ QDSSCs.

In the present work, we sensitized TiO$_2$ electrodes with QDs obtained by the SILAR technique, starting from aqueous solutions of Bi(NO$_3$)$_3$ as the cation precursor and Na$_2$S as the sulfide source. In a second variant, we used a similar procedure, but the Na$_2$S solution was replaced by elemental sulfur vapor as precursor. We found that an immersion time shorter than 30 min does not lead to an efficient QDs deposition into the TiO$_2$ porosities closer to the substrate. The obtained deposits were characterized by Raman scattering and diffuse reflectance spectroscopies, X-ray diffraction, and transmission electron microscopy (TEM). It was found that the presence of sodium ions in the reaction system does not directly lead to the formation of Bi$_2$S$_3$ on the porous TiO$_2$ layer. Additionally, the resulting nanostructured layers were tested as photoelectrodes. The current−voltage (J−V) characteristic and the photocurrent time stability revealed: (i) the much better performance of Bi$_2$S$_3$ QDs sensitized photoelectrodes obtained using elemental sulfur vapor as precursor and (ii) the inconvenience of sodium ions inclusion in the attempted synthesis procedure. A maximum conversion efficiency of 0.84% for Bi$_2$S$_3$ photo-electrochemical solar cells was reached in this work.

■ EXPERIMENTAL PROCEDURES

Reagents. Bismuth nitrate pentahydrate (Bi(NO$_3$)$_3$·5H$_2$O, Sigma, 98%), sodium sulfide nonahydrated (Na$_2$S·9H$_2$O, Fermont, analytical grade), cobalt nitrate (Co(NO$_3$)$_2$, Mallinckrodt, 99.76%), elemental sulfur (S, Sigma-Aldrich, 99.5%), sodium hydroxide (NaOH, J. T. Baker, 98.3%), titanium dioxide (TiO$_2$, AEROXIDE TiO$_2$-P25, Evonic, 99.5%), glacial acetic acid (CH$_3$COOH, J. T. Baker, 99.9%), and ethanol (CH$_3$CH$_2$OH, Analytyka 99.85%) were used. Ultrapure water (18 MΩ cm) was obtained from an Easypure

compact Ultra Barnstead deionization system. All chemicals were used without further purification.

TiO$_2$ Layer Deposition. Porous TiO$_2$ layers of about (10.2 ± 0.5) μm thick were deposited applying the doctor blade technique,[46] on fluorinated tin oxide covered glass (FTO, SnO$_2$:F, Solaronix TCO22-15, 15 Ω/sq) cut in pieces of 2 × 1.5 cm^2. For some experiments a glass substrate was used. The TiO$_2$ suspension was prepared by sonicating 4.0 g of the nanocrystalline TiO$_2$ powder AEROXIDE P25 (TiO$_2$-P25) with 1 mL of glacial acetic acid, until a viscous paste was formed (5 min), and then 15 mL of ethanol was added and the mixture was sonicated for 30 min. The TiO$_2$ layer annealing process was conducted at 450 °C for 30 min in air.

QDs Deposition. The SILAR technique was used for the deposition of the QDs on the surface of the nanoporous TiO$_2$ layer. In this method, successive immersions of the electrode into separate precursor solutions, intercalating washing procedures, produce an ionic layer precipitation effect.[47] The bismuth source consists of a Bi(NO$_3$)$_3$ aqueous solution. The immersion time of the TiO$_2$-P25 porous layer was 30 min, followed by a 1 min deionized water wash, and a drying process under an air flow. Different Bi(NO$_3$)$_3$ solution concentrations, from 2 × 10^{-4} M to 1 × 10^{-3} M, were used to vary the QDs sizes in different TiO$_2$ layers. Then, the Bi(III)-impregnated TiO$_2$ porous layer is immersed into a Na$_2$S aqueous solution with a concentration 1.5 times higher than that of the previous Bi(NO$_3$)$_3$ solution. The immersion time in the sulfide solution was also 30 min. Shorter immersion periods in the precursor solutions led to no appreciable QDs deposition close to the back side of photoelectrode: the front side gets a brown color, while the back side (close to the FTO) remains white. Also, shorter immersion times and many repetitions of these processes did not lead to a better QDs coverage of the back side of the TiO$_2$ porous layer. That is why we only used one SILAR process of 30 min, differing from the typical multiprocesses deposition.

A new variant of this technique was tried out, but using elemental sulfur vapor as precursor instead of Na$_2$S aqueous solutions. In this deposition path, the TiO$_2$ layer—previously impregnated in an aqueous solution of Bi(NO$_3$)$_3$, rinsed with water and dried under room conditions—is placed in a hermetically closed container (85 mL) with 0.05 g of elemental sulfur powder. This quantity fairly guarantees a molar sulfur excess with respect to Bi(III). Then, the temperature in the container is raised to 180 °C; at this stage all the elemental sulfur is in vapor phase. This thermal condition is held for 15 min. After that, the container is left to cool until it reaches room temperature. This method was also used to prepare cobalt sulfide on the FTO surface, for the counterelectrodes; in this case a 5 × 10^{-2} M Co(NO$_3$)$_2$ solution in ethanol was used as the precursor.

Nanopowder Preparation. A QDs colloid was obtained using synthesis conditions analogous to those used for the first solution-process variant, but no surface impregnation is involved. For that purpose, an aqueous solution reaction mixture of Bi(NO$_3$)$_3$·5H$_2$O (1 × 10^{-3} M) and Na$_2$S·9H$_2$O (1.5 × 10^{-3} M) was prepared, under vigorous stirring and room conditions; a solid brown precipitate was collected by centrifugation and washed with deionized water for further characterization.

Photoelectrochemical Cell Configuration. Photoelectrodes and counterelectrodes were separated by a Parafilm spacer that prevents direct contact between the electrodes, and it

retains the electrolyte in a sandwich-like configuration. The cell was pressed by two binder clips in the parallel edges of the structure, letting the electrical contacts free. The electrolyte contained in the interelectrode space was composed of 1 M S, 1 M $Na_2S \cdot 9H_2O$, and 0.1 M NaOH solved in deionized water.

Photocurrent−Voltage Measurements. The irradiation source used for the photocurrent−voltage (J−V) measurement was a 150 W arc xenon lamp (Osram XBO 150W/CR OFR), which roughly simulates the solar spectrum. An AM1.5 global filter (81094 Air Mass Filter, Newport) was used in the experiments. The incident light intensity was adjusted to 100 mW/cm^2 using a calibrated Si photodiode (ThorLabs SM05PD2B). The current−voltage curves were obtained by means of a Keithley Picoammeter/Voltage Source, model 6487, in the cells' steady state. At least three similar devices were considered in each characterization, and the average of the measured parameters and the corresponding standard deviations are presented.

Other Characterization Techniques Used. X-ray diffraction (XRD) patterns were taken on a Bruker D2-Phaser diffractometer equipment using Cu Kα radiation (10 mA, 30 kV, λ = 1.5418 Å) and an integration time of 0.5 s. High-resolution transmission electron micrographs (HR-TEM) were obtained using a JEM 2010 microscope equipped with a high-angle annular dark field detector, at a voltage of 200 kV. Diffused reflectance spectra were recorded on a Cary-5E Varian, and the Kubelka−Munk function was computed by the software. Raman spectra were recorded with a EZRaman-N (Enwave Optronics) Raman analyzer coupled to a Leica DM300 microscope with a 100× objective, using an excitation laser source of 532 nm wavelength and ~30 mW of output power.

■ RESULTS AND DISCUSSION

Figure 1a show the diffraction patterns of a naked TiO_2-P25 porous layer and that corresponding to an analogous TiO_2-P5 layer covered by the quantum dots deposited by the SILAR technique. As can be seen, only diffraction peaks corresponding to the anatase and rutile phases of TiO_2 appear in the diffraction patterns. As it is known, TiO_2-P25 presents around 70% of anatase and 30% rutile. The QDs-covered layer (Figure 1a) was obtained using 1×10^{-3} M $Bi(NO_3)_3$ and 1.5×10^{-3} M Na_2S solutions as precursors. Because of solubility limitations of $Bi(NO_3)_3$ in water at room conditions, 1×10^{-3} M was the maximum solution concentration of this salt used in the photoelectrodes preparation. The resulting layer was the darkest stain (brown) among those obtained by SILAR, so it is expected to have the highest QDs loading. The absence of peaks corresponding to Bi_2S_3, or any other sulfur compound, in this sample (Figure 1a) may be due to the amorphous character or the short-range crystalline order of the deposited nanostructures. No change was observed in the diffraction pattern of this sample after 45 min of thermal annealing, at 200 °C in air, nor in Argon. At longer times or higher temperatures, in air or argon, the samples suffered a significant discoloration indicating the QDs degradation.

It is noteworthy to mention that when attempting the analogous nanoparticles synthesis, but in aqueous colloidal suspension, using the same raw materials (1×10^{-3} M $Bi(NO_3)_3$ and 1.5×10^{-3} M Na_2S as final solution concentrations), the obtained product is a poorly crystalline $NaBiS_2$, Figure 1b. After a thermal annealing, at 160 °C in air for 30 min, the crystallinity of $NaBiS_2$ increased and its
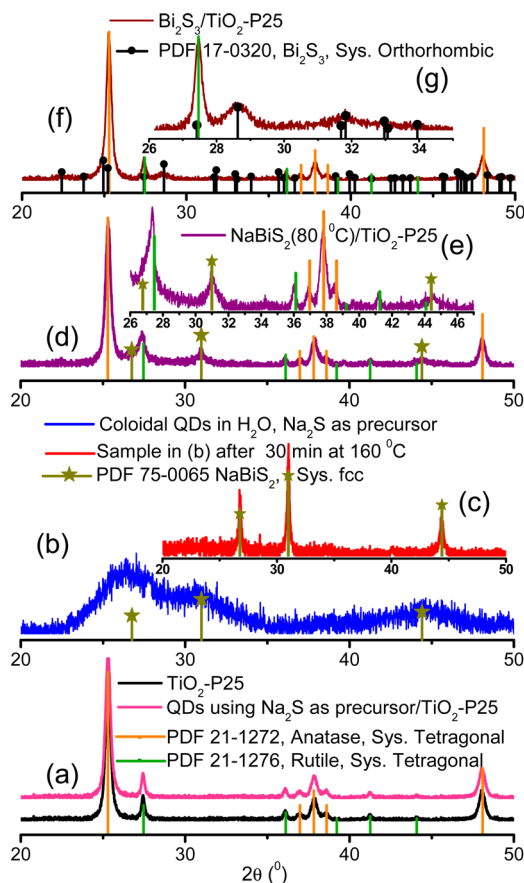
Figure 1. (a) Diffraction patterns of a naked TiO_2-P5 porous layer and a TiO_2-P5 layer covered with QDs obtained by SILAR using 1×10^{-3} M $Bi(NO_3)_3$ and 1.5×10^{-3} M Na_2S aqueous solutions as precursors. (b) Low crystalline $NaBiS_2$ obtained by the colloidal method from 1×10^{-3} M $Bi(NO_3)_3$ and 1.5×10^{-3} M Na_2S aqueous solution, (c) sample in (b) after a thermal annealing at 160 °C for 30 min in air, $NaBiS_2$ is now crystalline. (d) TiO_2-P5 layer covered with $NaBiS_2$ QDs obtained by SILAR, but using saturated precursor solutions at 80 °C. (e) Rerecorded diffraction pattern, between 26° and 47°, of the sample in (d), but using an integration time that is 7 times longer. (f) A TiO_2-P5 layer covered by Bi_2S_3 nanoparticles synthesized using a 1×10^{-3} M $Bi(NO_3)_3$ solution and elemental sulfur vapor as precursors. (c) Rerecorded diffraction pattern between 26° and 35° of the sample in (f), using an integration time that is 7 times longer.

diffraction peaks clearly matched the PDF 75-006, Figure 1c. The $NaBiS_2$ compound has been reported as a direct product of the reaction of Bi(III) salts with different S^{2-} sources in the presence of Na^{1+} ions, under hydrothermal conditions. This ternary compound yields Bi_2S_3 by a long decomposition process along the mentioned synthesis route.[48] Particularly, when using Na_2S as the sulfur source and having reaction times shorter than 3 h, amorphous $NaBiS_2$ is formed; a prolonged time is needed to completely form pure Bi_2S_3 (autoclave at 160 °C for 72 h).[48] The similar ionic radii of Na^{1+} (102 pm) and Bi(III) (103 pm), in combination with their unspecific and variable coordination chemistry, have been argued to explain the easy formation of different sodium−bismuth compounds.[49] The observed experimental facts, in the colloidal synthesis, suggest that a considerable presence of low crystalline or amorphous $NaBiS_2$ should be expected among the quantum dots deposited on TiO_2, when starting from Na_2S as the S^{2-} source.
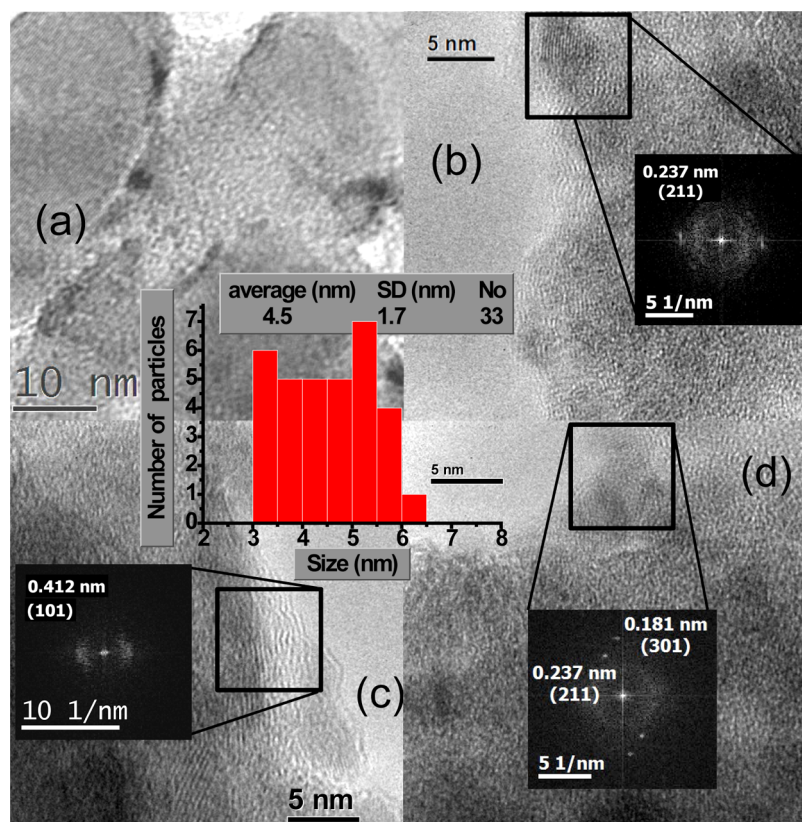
Figure 2. HR-TEM micrographs of a TiO$_2$ layer with QDs deposited on its surface, by SILAR, using aqueous solutions of Bi(NO$_3$)$_3$ (1 × 10^{-3} M) and M Na$_2$S (1.5 × 10^{-3}). The particle size distribution of the QDs deposited on the TiO$_2$ surface is inserted. The Supporting Information includes more TEM micrographs.

As the NaBiS$_2$ nanostructures could not be crystallized on the TiO$_2$ surface by direct SILAR processes at room conditions, nor by postsynthesis thermal annealing (first it degrades), saturated solutions of the precursors at 80 °C were tried. The diffraction pattern of the resulting sample is shown in Figure 1d. As can be seen, new broad peaks around 31.0° and 44.5° appeared this time, apart from those of the TiO$_2$-P25. This fact confirmed the deposition of NaBiS$_2$ on the TiO$_2$ surface under the present conditions. In order to obtain a better resolution of the NaBiS$_2$ diffraction peaks, the corresponding pattern was rerecorded (between 26° and 47°, see Figure 1e) using an integration time that is 7 times the one used in Figure 1d. It is important to mention that this NaBiS$_2$/TiO$_2$-P25 layer is easily detached from the FTO substrate by a simple water rinse, so it was not a useful synthesis route for photoelectrodes preparation.

The results presented so far indicate that the presence of sodium has to be carefully prevented in the reaction system (regarding pure Bi$_2$S$_3$ synthesis under soft reaction conditions). Particular attention must be paid when the synthesis of ternary compounds, like AgBiS$_2$, is attempted in the presence of sodium ions. AgBiS$_2$[50] and NaBiS$_2$[48] have very similar crystalline structures and show very close diffraction patterns. Lee et al.,[51] disregarding this point, claimed the sensitization of TiO$_2$ with AgBiS$_2$ using a reaction medium containing sodium ions. However, the diffraction patterns of the samples, before and after the annealing processes, match slightly better the PDF of NaBiS$_2$ (75-0065, quality: calculated) than that of the PDF used for AgBiS$_2$ identification (04-0699, quality: deleted). This important point of the structural characterization and its

possible impact on the obtained results were not discussed in ref 51. For further comments on different works, concerning unintentional formation of (BiS$_2$)$^{-1}$ compounds, see the Supporting Information.

To avoid the formation of NaBiS$_2$, the sulfide source (Na$_2$S) was replaced by elemental sulfur in the synthesis procedure, as it was described in the Experimental Section. This route prevents the presence of alkaline cations, which have also been reported as precursors for the formation of XBiS$_2$ type compounds (X = alkali metal cations).[52,53] The diffraction pattern of a sensitized layer, using a 1 × 10^{-3} M Bi(NO$_3$)$_3$ solution, for the Bi(III) surface impregnation, are shown in Figure 1f. Slight signals of orthorhombic Bi$_2$S$_3$ can be identified in Figure 1f, probably due to the small amount of QDs with respect to TiO$_2$. To improve the signal-to-noise ratio and better detect the Bi$_2$S$_3$ formation, the diffraction pattern of this sample was rerecorded (between 26° and 35°) using an integration time that is 7 times the one used in Figure 1f; this result is displayed in Figure 1g.

The QDs formed on the surface of the porous TiO$_2$ layer, using Na$_2$S as precursor, were analyzed by the HR-TEM technique, Figure 2. As can be seen in Figure 2a, some nanostructures (darker particles) are deposited on TiO$_2$-P25 nanocrystals (with lighter color). The poor crystallinity of the sensitizer can be noted in this micrograph; only lattice fingers of TiO$_2$ particles are observed. Those smaller and darker nanoparticles in Figure 2a are typically isolated from each other, although clusters of them can be observed in Figure 2b–d. It can be corroborated in Figure 2b–d (with higher resolution) that most of the deposited nanostructures have very low
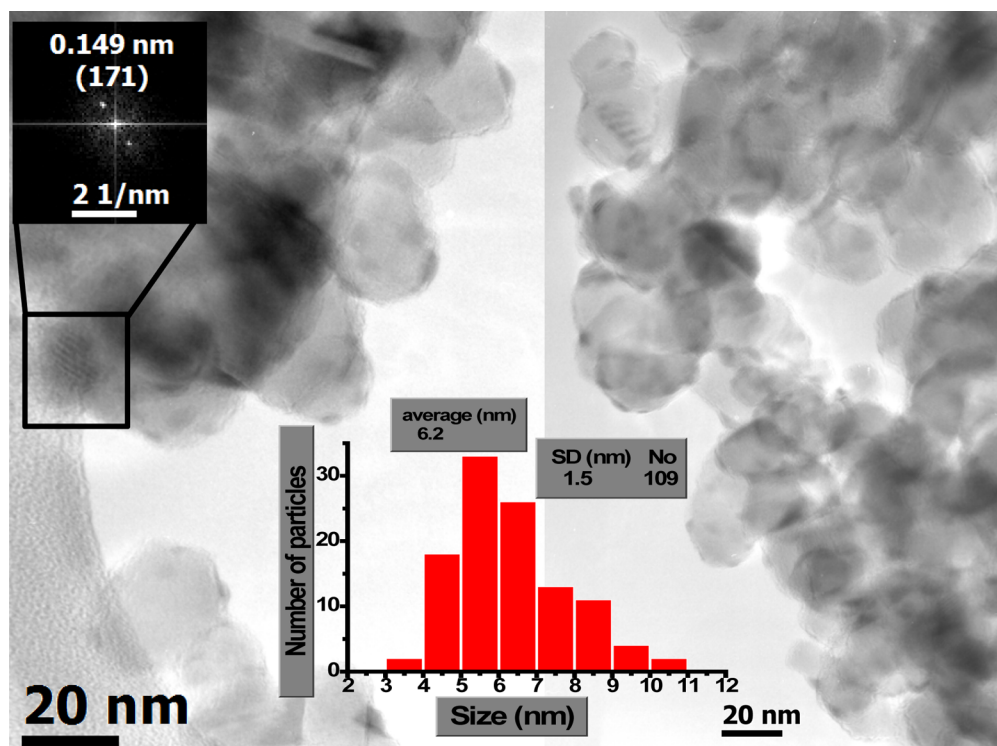
Figure 3. TEM micrographs of a Bi$_2$S$_3$/TiO$_2$-P5 sample prepared by SILAR using a 1 × 10^{-3} M Bi(NO$_3$)$_3$ solution and elemental sulfur vapor as precursors. The particle size distribution of the Bi$_2$S$_3$ QDs is included.

crystallinity. However, it was possible to find some particles showing more structural order; see Figure 2b,d. In Figure 2b the fast Fourier transform (FTT) of the squared zone revealed an interplanar distance of 0.237 nm, which perfectly matches that of the (211) plane of NaBiS$_2$. The FTT of the squared zone in Figure 2d showed interplanar distances of 0.237 and 0.181 nm corresponding to (211) and (301) planes of NaBiS$_2$, respectively. An amorphous-like structure is squared in Figure 2c. Because of this very short-range order, the corresponding FFT has an annular feature. The obtained radius is very close to 0.408 nm, which matches well with the intrerplanar distance of the (101) plane of NaBiS$_2$. These findings agree with the results observed by XRD. The interplanar distances of NaBiS$_2$ were computed with CaRIne v3.1 software; for more details see the Supporting Information. The resulting size distribution of the QDs is inserted in Figure 2, and an average size of 4.5 nm with a standard deviation (SD) of 1.7 nm was obtained.

TEM micrographs of a Bi$_2$S$_3$/TiO$_2$-P5 sample, prepared using a 1 × 10^{-3} M Bi(NO$_3$)$_3$ solution and elemental sulfur vapor as precursors, are presented in Figure 3. It can be appreciated that the Bi$_2$S$_3$ QDs (darker particles in the micrographs) are deposited on the surface of the TiO$_2$-P25 particles (20−30 nm, lighter color). Also, the Bi$_2$S$_3$ QDs are typically well dispersed. The Bi$_2$S$_3$ nanoparticles have an average size of 6.2 nm with a standard deviation of 1.5 nm. The FFT of the squared zone evidenced a 0.140 nm interplanar distance in the particle lattice, which belongs to the (171) plane of the Bi$_2$S$_3$ crystalline structure (PDF 17-0320). The Supporting Information includes more Bi$_2$S$_3$ particles identification.

Raman spectroscopy constitutes a powerful tool for the structural characterization of solid materials. The corresponding spectra of NaBiS$_2$/TiO$_2$-P25 samples, obtained with the precursor solutions at room temperature and those at 80 °C

(as in XRD analysis), and a Bi$_2$S$_3$/TiO$_2$-P25 layer, are shown in Figure 4. The spectrum of a naked TiO$_2$-P25 porous layer was
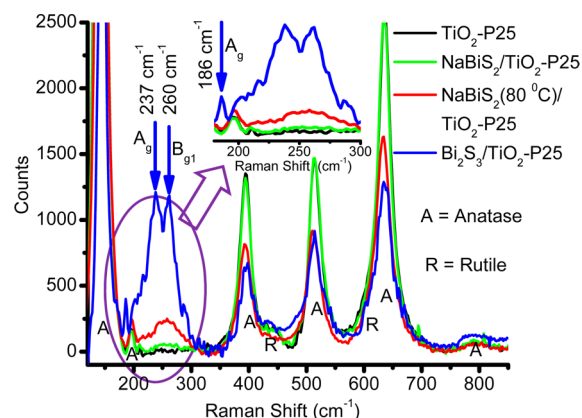
Figure 4. Raman scattering spectra of a naked TiO$_2$-P5 porous layer, a TiO$_2$-P5 layer covered by NaBiS$_2$ QDs (obtained by SILAR using 1 × 10^{-3} M Bi(NO$_3$)$_3$ and M 1.5 × 10^{-3} Na$_2$S solutions, at room temperature), NaBiS$_2$(80 °C)/TiO$_2$-P25 deposited using saturate precursor solutions at 80 °C and a TiO$_2$-P5 layer covered by Bi$_2$S$_3$ QDs (obtained by impregnating the substrate in a 1 × 10^{-3} M Bi(NO$_3$)$_3$ solution and using elemental S vapor). The blue arrows indicate Bi$_2$S$_3$ Raman mode positions.[54]

included as reference, and the bands related to the anatase and rutile TiO$_2$ phases are present in this and in the other samples. See the Supporting Information, for more details on the observed TiO$_2$ Raman signals. Additionally, the spectrum of the Bi$_2$S$_3$/TiO$_2$-P25 sample has the characteristic Bi$_2$S$_3$ strong signals at 237 and 260 cm^{-1} and the weak one at 186 cm^{-1}.[54] This is a signature of the crystalline character of the Bi$_2$S$_3$ QDs and its relative abundance, which is in accordance with XRD
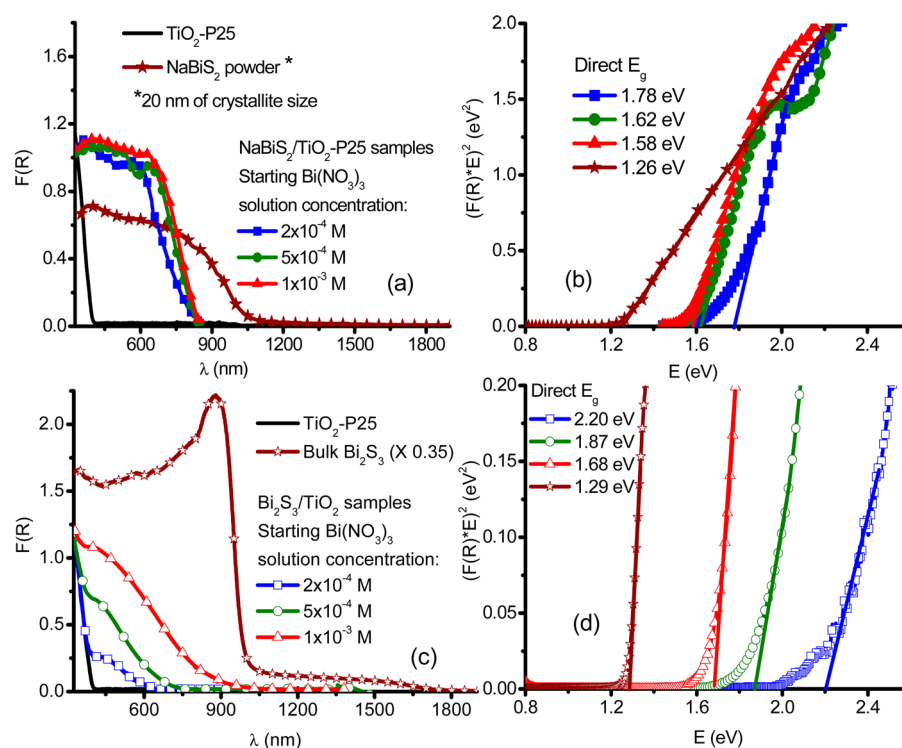
Figure 5. (a) Absorption spectra of different TiO_2 layers sensitized with $NaBiS_2$ quantum dots deposited under different conditions. (b) Plots for gap energy calculation from the spectra displayed in (a). (c) Absorption spectra of different TiO_2 layers sensitized with Bi_2S_3 quantum dots deposited under different reaction conditions. (d) Plots for gap energy calculation from the spectra in (c).

and TEM analysis. These results agree with those reported by Lutz et al.[55] The spectrum of the $NaBiS_2/TiO_2$-P25 obtained using precursor solutions at room temperature does not show new significant signals, apart from those of TiO_2. This is probably due to the poorly crystalline nature of these nanostructures; XRD and HR-TEM results accounted for the same fact. The $NaBiS_2/TiO_2$-P25 sample obtained with the saturated precursor solutions at 80 °C, which has a higher range of structural order (see Figure 1a,d), presents a broad Raman band between 200 and 320 cm^{-1}, with a maximum at 258 cm^{-1}. This band is located in the same wavenumber range where the most intense signals of Bi_2S_3 appear, but their spectral profile shapes are quite different. The $NaBiS_2/TiO_2$-P25 spectrum does not show any signal around the weak band of 186 cm^{-1} which belongs to Bi_2S_3. There is not a single previous report in the literature concerning the Raman spectrum of $NaBiS_2$. So, it was not possible to establish a comparison with a published reference spectrum. However, analogous results were obtained by comparing the Raman spectra presented here with those corresponding to crystalline $NaBiS_2$ and Bi_2S_3 nanoparticles produced by colloidal synthesis. For more details, see the Supporting Information.

Figure 5a shows the absorption spectra of the porous TiO_2 layers with adsorbed $NaBiS_2$ QDs of different sizes on its surface. The spectrum of a naked TiO_2 layer and that of a $NaBiS_2$ powder sample (its X-RD pattern is in Figure 1c) were also added for comparison. The concentration of the $Bi(NO_3)_3$ aqueous solutions used in the deposition process was varied from 2×10^{-4} to 1×10^{-3} M, as it is indicated in the figure legend. As can be seen, the absorption spectra show a blue shift when lower precursor concentrations are used. This is a consequence of the smaller particle size obtained in these conditions. The higher values of gap energies, with decreasing

particle size of sensitizer, are a consequence of the quantum confinement (Figure 5b). The gap energy of the $NaBiS_2$ powder, the one with the largest crystallite size obtained here (20 nm), is 1.26 eV. This is the first time that experimental band gap energy values of $NaBiS_2$ are reported.

The absorption spectra of the TiO_2 layers sensitized with Bi_2S_3 are shown in Figure 5c. The spectra of a naked TiO_2 layer and that corresponding to a bulk Bi_2S_3 sample are included as references. Again, the concentration of the Bi(III) precursor solutions, used in the impregnation process, was varied from 2×10^{-4} to 1×10^{-3} M. The Bi_2S_3 QDs, obtained with the highest concentration of the Bi(III) salt, have a broader absorption spectral range than the analogous $NaBiS_2$ nanostructures. It can be noted that the intensity of the absorption spectra of the QDs monotonically grows with the increasing of the Bi(III) precursor concentration (see the shoulder around 450 nm as a reference). This fact suggests a smaller QDs loading as the concentration of the precursor solution is decreased. In addition, the blue shift of the spectrum corresponding to Bi_2S_3 QDs is more prominent than that observed in $NaBiS_2$.

The direct band gap energy obtained for bulk Bi_2S_3 is 1.29 eV, which is very close to the value of 1.3 eV reported by some authors,[1,6,7] but differs from that of some others.[7-9] The observed blue shift in the E_g values (Figure 5d) indicates the charge carriers' confinement. It is possible to approximately calculate the size of the Bi_2S_3 QDs from the band gap energy blue shift with respect to the bulk material value. In that concern, the Brus model,[56] based on the effective mass approximation, is close to its validity limit in our Bi_2S_3 nanocrystals (particle size ≫ lattice parameters, 10 times larger is a practical value).[57] So, we instead used the more general Wang model[57] to estimate the particle size from the

corresponding band gap value. Wang derived the following E_g dependence on the particle radius (R), based on a hyperbolic band model: $E_g = [E_{g0}{}^2 + 2\hbar^2 E_g (\pi/R)^2/\mu^*]^{1/2}$; where E_{g0} is the bulk band gap value and μ^* is the reduced effective mass of the exciton.[57] For the calculation, we need the reduced effective mass of the exciton in Bi_2S_3. Considering the anisotropic character of Bi_2S_3, average values for the reduced effective mass have been reported between 0.01 and 0.7 times the free electron mass (m_0).[8,58] However, none of those informed μ^* values fit well to our experimental result of $E_g = 1.68$ eV for an average particle size of 6.2 nm (using Wang's relation). So, we decided to calculate the Bi_2S_3 reduced effective mass, using the mentioned experimental E_g and particle size of one of our samples; 0.18 m_0 was obtained as the adequate μ^* value for the Bi_2S_3 QDs of this work. Then, with this more realistic μ^*, $E_{g0} = 1.3$ eV, and the different E_g obtained from the absorption spectra, the average sizes of the corresponding Bi_2S_3 nanoparticles were estimated. Also, using this μ^* value, the Bi_2S_3 Bohr radius was calculated, and the result is 19.5 nm; this value is about 1.5 times shorter than that reported by Pejova et al.[8] Finally, the results of the Bi_2S_3 QDs sizes estimation are shown in Table 1.

Table 1. Calculated Bi_2S_3 QDs Sizes, from the Corresponding Gap Energy Values[a]

	[Bi(III)] (M)	E_g (eV)	calculated size (nm)
Bi_2S_3 QDs	1×10^{-3}	1.68 ± 0.07	6.2 ± 1.5 (TEM)
	5×10^{-4}	1.87 ± 0.07	4.9 ± 1.2 (W)
	2×10^{-4}	2.20 ± 0.07	3.7 ± 0.9 (W)

[a]The errors in E_g calculations are included in the respective table cell. [Bi(III)] stands for the Bi(III) precursor solutions concentration used in the sample preparation, and W indicates the size values which were derived from the E_g blue-shift, using the Wang's relation.[57] Particularly, for the sample with [Bi(III)] = 1×10^{-3} M the average size displayed is that obtained from TEM micrographs (TEM), its standard deviation is presented as error. Strictly speaking, the error in W calculations is 0.4 nm; however, we have decided to include as error a value that considers the effect of sized dispersion of the [Bi(III)] = 1×10^{-3} M sample on the parameters derived from it, used in the W approach for the rest of the samples.

An analogous estimation for the $NaBiS_2$ nanoparticles average sizes was not possible because of the lack of information about the optical constants and the charge carriers effective mass of this material in the literature.

Figure 6a shows the average current−voltage characteristic of the photoelectrochemical solar cells using $NaBiS_2/TiO_2$-P25 photoelectrodes, with different quantum dot sizes. The concentration of the $Bi(NO_3)_3$ precursor solutions, used in the fabrication of the corresponding photoelectrodes, are indicated in the inserted legend. Table 2 shows the photovoltaic parameters of the different solar cells (curves in Figure 6a). As can be seen in Figure 6a and in Table 2, the smaller the $NaBiS_2$ QD size the higher the cell efficiency. That means that electron injection, from $NaBiS_2$ to TiO_2, increases for the smaller particles due to the favorable relatively positions of their respectively conduction bands. The increasing tendency of the cells efficiencies suggest that the $NaBiS_2$ optimal size was not found yet, but it would be smaller than 4.5 nm; research is still in progress. The fill factors did not significantly change from one cell to another, and the values are relatively low, indicating a high recombination rate in these systems. It is important to mention that photoelectrodes submitted to thermal annealing
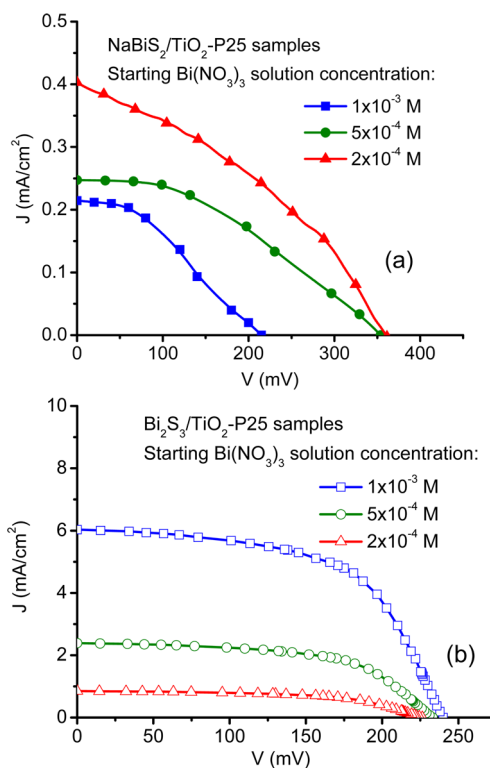
Figure 6. Average current−voltage characteristic of photoelectrochemical solar cells, using different QD sizes in the (a) $NaBiS_2/TiO_2$-P25 and (b) Bi_2S_3/TiO_2-P25 photoelectrodes. At least three devices of each type were measured.

at 150, 175, and 200 °C, for 30 min in air, show a very slight efficiency diminishment but no significant differences.

The average current−voltage characteristics of cells, sensitized by Bi_2S_3 QDs of different sizes, are shown in Figure 6b. Once again, the concentration of the Bi(III) precursor solutions, corresponding to the fabrication of the photoelectrodes, are indicated in the inserted legend. The photovoltaic parameters of the different solar cells (extracted from curves in Figure 6b) are shown in Table 2. As can be seen, a considerable increment of about 1 order of magnitude, in the conversion efficiency, was observed in comparison with the analogous cells using $NaBiS_2$ QDs as sensitizers. This fact suggests a probable slower recombination rate when using the Bi_2S_3 QDs, which are more crystalline than the $NaBiS_2$ nanostructures. It is important to mention that the heating in the synthesis procedure might not only favor the crystallinity of the Bi_2S_3 QDs, but also its tighter contact onto the TiO_2 surface. Also, a better energy band alignment and/or a higher sensitizers loading could favor the better performance, in the case of Bi_2S_3 QDs sensitized solar cells. The short circuit photocurrent and the fill factor were the most relevantly improved parameters with respect to the case of $NaBiS_2$. These parameters values are among the highest reported for any Bi_2S_3 QDs sensitized solar cell to date. The larger the size of the Bi_2S_3 QDs, up to 6.2 nm in our study, the higher the cell efficiency. Despite the fact that the cell design was not optimized—the cells are not hermetically closed, the electrical contacts were not silver painted, compact blocking layers were not used, the TiO_2 porous layer structure does not have an optimized porosity and thickness nor light diffusing elements[59]—the efficiency of 0.84% is the highest value found in the literature for any Bi_2S_3 photoelectrochemical solar cell. The performance of the cells

Table 2. Average Photovoltaic Parameters of Photoelectrochemical Solar Cells, Using Different Quantum Dot Sizes in the NaBiS$_2$/TiO$_2$-P25 and Bi$_2$S$_3$/TiO$_2$-P25 Photoelectrodes[a]

	[Bi(III)] (M)	QD size (nm)	I_{sc} (mA/cm^2)	V_{oc} (mV)	FF	η (%)
NaBiS$_2$ QDSSC	1×10^{-3}	4.5 ± 1.7 (TEM)	0.21 ± 0.03	215 ± 5	0.36 ± 0.05	0.016 ± 0.006
	5×10^{-4}		0.25 ± 0.03	352 ± 8	0.38 ± 0.07	0.033 ± 0.011
	2×10^{-4}		0.40 ± 0.04	354 ± 8	0.37 ± 0.05	0.052 ± 0.013
Bi$_2$S$_3$ QDSSC	1×10^{-3}	6.2 ± 1.5 (TEM)	6.03 ± 0.11	240 ± 7	0.58 ± 0.05	0.84 ± 0.11
	5×10^{-4}	4.9 ± 1.2 (W)	2.39 ± 0.12	233 ± 8	0.57 ± 0.06	0.32 ± 0.06
	2×10^{-4}	3.7 ± 0.9 (W)	0.85 ± 0.09	225 ± 7	0.57 ± 0.07	0.11 ± 0.03

[a]At least three devices of each type were measured. The standard deviation from the measured photovoltaic parameters average is included. [Bi(III)] stands for the Bi(III) precursor solutions concentration used in the sample preparation. W and TEM are the same as in Table 1.

might also be improved by passivating the QDs surface; ZnS, CdS and SiO$_2$ have been successfully applied in other systems for that purpose.[59] Molecular dipoles can also improve the electron injection efficiency.[59] Another important element that has to be optimized is the counterelectrode; in this study we observed that Na impurities in the synthesis procedure, crystalline phase, and the particle size of the cobalt sulfide strongly affect the catalytic activity of the counterelectrode in contact with the polysulfide electrolyte; research is still in progress.

In order to test the stability of the cells, the short circuit photocurrent density versus time was measured for the best cells of both types of sensitizers; see Figure 7. The irradiation
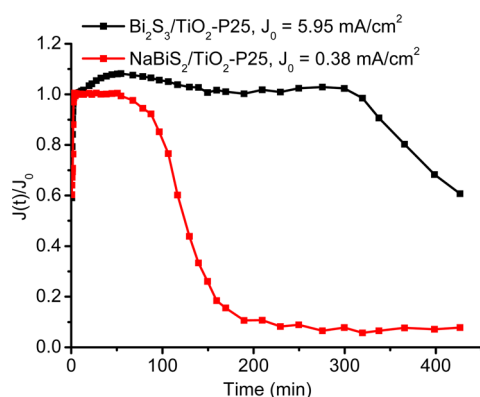
Figure 7. Time dependent photocurrent density of solar cells sensitized with Bi$_2$S$_3$ or NaBiS$_2$ QDs. J_0 is the "steady state" short circuit photocurrent; that value is reached by the cells in about 2 min (after starting the irradiation), and it is held no further than 5% from its value, for at least 15 min.

condition is the same to that of the J−V measurement. As can be seen, the photocurrent of the cell using Bi$_2$S$_3$ QDs was relatively stable for about 5 h, and then it started to drop, probably due to the oxidation of the electrolyte (the cell is not hermetically closed). It was verified that the electrolyte is oxidized after about 5 h of aging in the sandwich-like structure of the cell used; see the Supporting Information. No significant change was detected in the average absorption spectrum of this photoelectrode, after this test. That indicates minimal photocorrosion of the Bi$_2$S$_3$ QDs. When using NaBiS$_2$ QDs as sensitizer, the photocurrent remained stable only for about 1 h, and a visible discoloration of the photoelectrode took place. This fact is in accordance with the observed attenuation of the electronic absorption and the Raman signals of the NaBiS$_2$ sensitized TiO$_2$ layers after this test; for more details see the Supporting Information. Vogel et al.[36] also reported a rapid

photodegradation (within minutes) in QDs obtained by 1 min SILAR, using saturated Bi(NO$_3$)$_3$ and 0.5 M Na$_2$S aqueous precursor solutions on TiO$_2$ porous layers. These facts and the previous results presented in this work support the hypothesis that these authors[36] basically obtained NaBiS$_2$ QDs.

The lack of information about thermodynamic, optical, and electrical parameters of NaBiS$_2$, in the literature, makes impossible a direct comparison with Bi$_2$S$_3$ in relation with the stability of these materials. A possible explanation for the observed lower stability of the NaBiS$_2$ amorphous nanostructures compared with the crystalline Bi$_2$S$_3$ QDs is as follows. Structural disorder, associated with the amorphous nature of the deposited NaBiS$_2$ QDs, turns them into nanostructures with a defect-rich lattice. The higher density of lattice strains, dangling bonds, dislocations, and some others defects can confer a higher reactive character and a lower stability to NaBiS$_2$, compared with the crystalline Bi$_2$S$_3$ QDs. Amorphous chalcogenide semiconductors are known to be structurally disordered, thermodynamically in nonequilibrium, and kinetically unstable materials.[60] Typically, those amorphous chalcogenides drastically change their physicochemical state by illumination and/or thermal annealing processes.[60] In this work we observed both thermal and illumination instabilities of the deposited amorphous NaBiS$_2$ nanostructures. Additionally, the hole accumulation on the surface of chalcogenide semiconductors has been identified as a corrosion inducing factor.[37] Probably, the amorphous NaBiS$_2$ nanostructures also have slower kinetics of hole transfer to the electrolyte than crystalline Bi$_2$S$_3$ QDs.

■ CONCLUSIONS

Using Bi(NO$_3$)$_3$ as a bismuth precursor and Na$_2$S as a sulfur source, in the SILAR technique, low crystalline NaBiS$_2$ QDs are obtained as the main product on the surface of the TiO$_2$ nanoporous layers. This result contrasts with what has been claimed by other authors.[36,37,45] New insights related with the lattice spacing and the Raman spectrum of NaBiS$_2$ were disclosed. Replacing Na$_2$S by elemental sulfur vapor, in the deposition procedure, crystalline Bi$_2$S$_3$ QDs are obtained. In our synthesis conditions, an immersion time shorter than 30 min does not favor the QDs deposition on the TiO$_2$ porous layer side close to the substrate; this situation persists even when many repetitions of 1 min immersion are performed. The solar cells, using photoelectrodes sensitized by Bi$_2$S$_3$ QDs, reached an efficiency 1 order of magnitude higher than the one using the low crystalline NaBiS$_2$, which are also less stable over time. A maximum efficiency of 0.84% was obtained when Bi$_2$S$_3$ QDs sensitized cells were used, which constitutes the highest value reported for any photoelectrochemical cell using this nanomaterial as an absorber. However, this value can be

11502

dx.doi.org/10.1021/jp411516a | J. Phys. Chem. C 2014, 118, 11495−11504

overcome by optimizing various parameters of the cell, such as the size of the QDs, the photoelectrode porosity, the surface passivation, the hermetic sealing of the cell, and a dip study of cobalt sulfide counterelectrode. Research is in progress.

■ ASSOCIATED CONTENT

Ⓢ Supporting Information

S1. Discussion on works using Bi_2S_3 as sensitizer. S2. Different works concerning unintentional formation of $(BiS_2)^{-1}$ compounds. S3. TEM analysis of a $NaBiS_2/TiO_2$-P25 and a Bi_2S_3/TiO_2-P25 samples. S4. Raman analysis of TiO_2, $NaBiS_2$, and Bi_2S_3. S5. $NaBiS_2/TiO_2$-P25 photoelectrodes and polysulfide electrolyte degradation evidence. S7. $NaBiS_2$ lattice spacing calculation. This material is available free of charge via the Internet at http://pubs.acs.org

■ AUTHOR INFORMATION

Corresponding Author

*E-mail: david@unam.mx. Phone and Fax: +52 55 5622-3813.

Notes

The authors declare no competing financial interest.

■ ACKNOWLEDGMENTS

■ REFERENCES

(1) Biswas, K.; Zhao, L.-D.; Kanatzidis, M. G. Tellurium-Free Thermoelectric: The Anisotropic n-Type Semiconductor Bi_2S_3. *Adv. Energy Mater.* **2012**, *2*, 634–638.

(2) Konstantatos, G.; Levina, L.; Tang, J.; Sargent, E. H. Sensitive Solution-Processed Bi_2S_3 Nanocrystalline Photodetectors. *Nano Lett.* **2008**, *8*, 4002–4006.

(3) Xi, Y.; Hu, C.; Zhang, X.; Zhang, Y.; Wang, Z. L. Optical Switches Based on Bi_2S_3 Nanowires Synthesized by Molten Salt. *Solid State Commun.* **2009**, *149*, 1894–1896.

(4) Brahimi, R.; Bessekhouad, Y.; Bouguelia, A.; Trari, M. Visible Light Induced Hydrogen Evolution over the Heterosystem Bi_2S_3/TiO_2. *Catal. Today* **2007**, *122*, 62–65.

(5) Yousefi, M.; Sabet, M.; Salavati-Niasari, M.; Emadi, H. Synthesis and Characterization PbS and Bi_2S_3 Nanostructures via Microwave Approach and Investigation of their Behaviors in Solar Cell. *J. Cluster Sci.* **2012**, *23*, 511–525.

(6) Patrick, C. E.; Giustino, F. Structural and Electronic Properties of Semiconductor-Sensitized Solar-Cell Interfaces. *Adv. Funct. Mater.* **2011**, *21*, 4663–4667.

(7) Larson, P.; Greanya, V. A.; Tonjes, W. C.; Liu, R.; Mahanti, S. D. Electronic Structure of Bi_2X_3 (X = S, Se, T) Compounds: Comparison of Theoretical Calculations with Photoemission Studies. *Phys. Rev. B* **2002**, *65*, 085108.

(8) Pejova, B.; Grozdanov, I. Structural and Optical Properties of Chemically Deposited Thin Films of Quantum-Sized Bismuth(III) Sulfide. *Mater. Chem. Phys.* **2006**, *99*, 39–49.

(9) Grigas, J.; Talik, E.; Lazauskas, V. X-ray Photoelectron Spectra and Electronic Structure of Bi_2S_3 Crystals. *Phys. Status Solidi B* **2002**, *232*, 220–230.

(10) Shockley, W.; Queisser, H. J. Detailed Balance Limit of Efficiency of p-n Junction Solar Cells. *J. Appl. Phys.* **1961**, *32*, 510–519.

(11) Cademartiri, L.; Malakooti, R.; O'Brien, P. G.; Migliori, A.; Petrov, S.; Kherani, N. P.; Ozin, G. A. Large-Scale Synthesis of Ultrathin Bi_2S_3 Necklace Nanowires. *Angew. Chem., Int. Ed.* **2008**, *47*, 3814–3817.

(12) Wang, Z. J.; Qu, S. C.; Xu, Y.; Chen, Y. H.; Zeng, X. B.; Liu, J. P.; Wu, J.; Wang, Z. G. Solventless Synthesis of Bi_2S_3 Nanowires and Their Application to Solar Cells. *Adv. Mater. Res.* **2007**, *26–28*, 601–607.

(13) Moreno-García, H.; Nair, M. T. S.; Nair, P. K. Chemically Deposited Lead Sulfide and Bismuth Sulfide Thin Films and Bi_2S_3/PbS Solar Cells. *Thin Solid Films* **2011**, *519*, 2287–2295.

(14) Becerra, D.; Nair, M. T. S.; Nair, P. K. Analysis of a Bismuth Sulfide/Silicon Junction for Building Thin Film Solar Cells. *J. Electrochem. Soc.* **2011**, *158*, H741–H749.

(15) Bhattacharya, R. N.; Pramanik, P. Semiconductor Liquid Junction Solar Cell Based on Chemically Deposited Bi_2S_3. Thin Film and Some Semiconducting Properties of Bismuth Chalcogenides. *J. Electrochem.* **1982**, *129*, 332–335.

(16) Mane, R. S.; Desa, J. D.; Joo, O.-S.; Han, S.-H. Surface Morphology and Optical Studies of Non-aqueous Bi_2S_3 Thin Films. *Int. J. Electrochem. Sci.* **2007**, *2*, 141–148.

(17) Rajalakshmi, P. U.; Oommen, R.; Sanjeeviraja, C. Improved Photoelectrochemical Performance of $(Bi_{1-x}Sb_x)_2S_3$ Photoanodes. *Thin Solid Films* **2013**, *531*, 76–80.

(18) Narayanan, R.; Deepa, M.; Friebel, F.; Srivastava, A. K. A CdS/Bi_2S_3 Bilayer and a Poly(3,4-ethylenedioxythiophene)/S^{2-} Interface Control Quantum Dot Solar Cell Performance. *Electrochim. Acta* **2013**, *105*, 599–611.

(19) Jana, A.; Bhattacharya, C.; Sinha, S.; Datta, J. Study of the Optimal Condition for Electroplating of Bi_2S_3 Thin Tilms and their Photoelectrochemical Characteristics. *J. Solid State Electrochem.* **2009**, *13*, 1339–1350.

(20) Kamat, P. V. Quantum Dot Solar Cells. Semiconductor Nanocrystals as Light Harvesters. *J. Phys. Chem. C* **2008**, *112*, 18737–18753.

(21) Kamat, P. V. Quantum Dot Solar Cells. The Next Big Thing in Photovoltaics. *J. Phys. Chem. Lett.* **2013**, *4*, 908–918.

(22) Kramer, I. J.; Sargent, E. H. The Architecture of Colloidal Quantum Dot Solar Cells: Materials to Devices. *Chem. Rev.* **2014**, *114*, 863–882.

(23) Wang, J.; Mora-Seró, I.; Pan, Z.; Zhao, K.; Zhang, H.; Feng, Y.; Yang, G.; Zhong, X.; Bisquert, J. Core/Shell Colloidal Quantum Dot Exciplex States for the Development of Highly Efficient Quantum-Dot-Sensitized Solar Cells. *J. Am. Chem. Soc.* **2013**, *135*, 15913–15922.

(24) Maraghechi, P.; Labelle, A. J.; Kirmani, A. R.; Lan, X.; Adachi, M. M.; Thon, S. M.; Hoogland, S.; Lee, A.; Ning, Z.; Fischer, A.; Amassian, A.; Sargent, E. H. The Donor-Supply Electrode Enhances Performance in Colloidal Quantum Dot Solar Cells. *ACS Nano* **2013**, *7*, 6111–6116.

(25) Wallentin, J.; Anttu, N.; Asoli, D.; Huffman, M.; Åberg, I.; Magnusson, M. H.; Siefer, G.; Fuss-Kailuweit, P.; Dimroth, F.; Witzigmann, B. InP Nanowire Array Solar Cells Achieving 13.8% Efficiency by Exceeding the Ray Optics Limit. *Science* **2013**, *339*, 1057–1060.

(26) Rath, A. K.; Bernechea, M.; Martinez, L.; Konstantatos, G. Solution-Processed Heterojunction Solar Cells Based on p-type PbS Quantum Dots and n-type Bi_2S_3 Nanocrystals. *Adv. Mater.* **2011**, *23*, 3712–3717.

(27) Robel, I.; Subramanian, V.; Kuno, M.; Kamat, P. V. Quantum Dot Solar Cells. Harvesting Light Energy with CdSe Nanocrystals Molecularly Linked to Mesoscopic TiO_2 Films. *J. Am. Chem. Soc.* **2006**, *128*, 2385−2393.

(28) Kongkanand, A.; Tvrdy, K.; Takechi, K.; Kuno, M.; Kamat, P. V. Quantum Dot Solar Cells. Tuning Photoresponse through Size and Shape Control of CdSe-TiO_2 Architecture. *J. Am. Chem. Soc.* **2008**, *130*, 4007−4015.

(29) Lee, H. J.; Yum, J.-H.; Leventis, H. C.; Zakeeruddin, S. M.; Haque, S. A.; Chen, P.; Seok, S. I.; Grätzel, M.; Nazeeruddin, Md. K. CdSe Quantum Dot-Sensitized Solar Cells Exceeding Efficiency 1% at Full-Sun Intensity. *J. Phys. Chem. C* **2008**, *112*, 11600−11608.

(30) Mora-Seró, I.; Giménez, S.; Moehl, T.; Fabregat-Santiago, F.; Lana-Villareal, T.; Gómez, R.; Bisquert, J. Factors Determining the Photovoltaic Performance of a CdSe Quantum Dot Sensitized Solar Cell: the Role of the Linker Molecule and of the Counter Electrode. *Nanotechnology* **2008**, *19*, 424007−424014.

(31) Timp, B. A.; Zhu, X.-Y. Electronic Energy Alignment at the PbSe Quantum Dots/ZnO(1010) Interface. *Surf. Sci.* **2010**, *604*, 1335−1341.

(32) Yu, K.; Chen, J. Enhancing Solar Cell Efficiencies through 1-D Nanostructures. *Nanoscale Res. Lett.* **2009**, *4*, 1−10.

(33) Leventis, H. C.; O'Mahony, F.; Akhtar, J.; Afzaal, M.; O'Brien, P.; Haque, S. A. Transient Optical Studies of Interfacial Charge Transfer at Nanostructured Metal Oxide/PbS Quantum Dot/Organic Hole Conductor Heterojunctions. *Am. Chem. Soc.* **2010**, *132*, 2743−2750.

(34) Dittrich, T.; Belaidi, A.; Ennaoui, A. Concepts of Inorganic Solid-State Nanostructured Solar Cells. *Sol. Energy Mater. Sol. Cells* **2011**, *95*, 1527−1536.

(35) Selinsky, R. S.; Ding, Q.; Faber, M. S.; Wright, J. C.; Jin, S. Quantum Dot Nanoscale Heterostructures for Solar Energy Conversion. *Chem. Soc. Rev.* **2013**, *42*, 2963−2985.

(36) Vogel, R.; Hoyer, P.; Weller, H. Quantum-Sized PbS, CdS, Ag_2S, Sb_2S_3, and Bi_2S_3 Particles as Sensitizers for Various Nanoporous Wide-Bandgap Semiconductors. *J. Phys. Chem.* **1994**, *98*, 3183−3188.

(37) Suarez, R.; Nair, P. K.; Kamat, P. V. Photoelectrochemical Behavior of Bi_2S_3 Nanoclusters and Nanostructured Thin Films. *Langmuir* **1998**, *14*, 3236−3241.

(38) Peter, L. M.; Wijayantha, K. G. U.; Riley, D. J.; Waggett, J. P. Band-Edge Tuning in Self-Assembled Layers of Bi_2S_3 Nanoparticles Used To Photosensitize Nanocrystalline TiO_2. *J. Phys. Chem. B* **2003**, *107*, 8378−8381.

(39) Calva, J. C.; Rincón, M. E.; Solís, M.; Alvarado, G. Photoelectrochemical Characterization of CNT-TiO_2 Electrodes Sensitized with Bi_2S_3. *ECS Trans.* **2011**, *36*, 581−589.

(40) Cai, F.-G.; Yang, F.; Jia, Y.-F.; Ke, C.; Cheng, C.-H.; Zhao, Y. Bi_2S_3-Modified TiO_2 Nanotube Arrays: Easy Fabrication of Heterostructure and Effective Enhancement of Photoelectrochemical Property. *J. Mater. Sci.* **2013**, *48*, 6001−6007.

(41) Pan, Z. X.; Zhao, K.; Wang, J.; Zhang, H.; Feng, Y. Y.; Zhong, X. H. Near Infrared Absorption of $CdSe_xTe_{1-x}$ Alloyed Quantum Dot Sensitized Solar Cells with More than 6% Efficiency and High Stability. *ACS Nano* **2013**, *7*, 5215−5222.

(42) Santra, P. K.; Kamat, P. V. Mn-Doped Quantum Dot Sensitized Solar Cells: A Strategy to Boost Efficiency over 5%. *J. Am. Chem. Soc.* **2012**, *134*, 2508−2511.

(43) Yan, K.; Chen, W.; Yang, S. Significantly Enhanced Open Circuit Voltage and Fill Factor of Quantum Dot Sensitized Solar Cells by Linker Seeding Chemical Bath Deposition. *J. Phys. Chem. C* **2013**, *117*, 92−99.

(44) Lee, J.-W.; Son, D.-Y.; Ahn, T. K.; Shin, H.-W.; Kim, I. Y.; Hwang, S.-J.; Ko, M. J.; Sul, S.; Han, H.; Park, N.-G. Quantum-Dot-Sensitized Solar Cell with Unprecedentedly High Photocurrent. *Sci. Rep.* **2013**, *3*, 1050.

(45) Lin, Y.-C.; Lee, M.-W. Bi_2S_3 Liquid-Junction Semiconductor-Sensitized SnO_2 Solar Cells. *J. Electrochem. Soc.* **2014**, *161*, H1−H5.

(46) Smestad, G. P.; Gratzel, M. Demonstrating Electron Transfer and Nanotechnology: A Natural Dye-Sensitized Nanocrystalline Energy Converter. *J. Chem. Educ.* **1998**, *75*, 752−756.

(47) Kamat, P. V.; Tvrdy, K.; Baker, D. R.; Radich, J. G. Beyond Photovoltaics: Semiconductor Nanoarchitectures for Liquid-Junction Solar Cells. *Chem. Rev.* **2010**, *110*, 6664−6688.

(48) Liu, Z.; Liang, J.; Li, S.; Peng, S.; Qian, Y. Synthesis and Growth Mechanism of Bi_2S_3 Nanoribbons. *Chem.—Eur. J.* **2004**, *10*, 634−640.

(49) Mehring, M. From Molecules to Bismuth Oxide-Based Materials: Potential Homo- and Heterometallic Precursors and Model Compounds. *Coord. Chem. Rev.* **2007**, *251*, 974−1006.

(50) Guin, S. N.; Biswas, K. Cation Disorder and Bond Anharmonicity Optimize the Thermoelectric Properties in Kinetically Stabilized Rocksalt $AgBiS_2$ Nanocrystals. *Chem. Mater.* **2013**, *25*, 3225−3231.

(51) Huang, P.-C.; Yang, W.-C.; Lee, M.-W. $AgBiS_2$. Semiconductor-Sensitized Solar Cells. *J. Phys. Chem. C* **2013**, *117*, 18308−18314.

(52) Gabrelyan, B. V.; Lavrentiev, A. A.; Nikiforov, I. Y.; Sobolev, V. V. Electronic Energy Structure of $MBiS_2$ (M = Li, Na, K) Calculated with Allowance for the Difference Between the M-S and Bi-S Bond Lengths. *J. Struct. Chem.* **2008**, *49*, 788−794.

(53) McCarthy, T. J.; Ngeyi, S. P.; Liao, J. H.; DeGroot, D. C.; Hogan, T.; Kannewurf, C. R.; Kanatzidis, M. G. Molten Salt synthesis and Properties of Three New Solid-State Ternary Bismuth Chalcogenides, Beta-$CsBiS_2$, Gamma-$CsBiS_2$, and $K_2Bi_8Se_{13}$. *Chem. Mater.* **1993**, *5*, 331−340.

(54) Zhao, Y.; Eddie- Chua, T. K.; Gan, C. K.; Zhang, J.; Peng, B.; Peng, Z.; Xiong, Q. Phonons in Bi_2S_3 Nanostructures: Raman Scattering and First-Principles Studies. *Phys. Rev. B* **2011**, *84*, 205330.

(55) Lutz, T.; MacLachlan, A.; Sudlow, A.; Nelson, J.; Hill, M. S.; Molloy, K. C.; Haque, S. A. Thermal Decomposition of Solution Processable Metal Xanthates on Mesoporous Titanium Dioxide Films: A New Route to Quantum-Dot Sensitized Heterojunctions. *Phys. Chem. Chem. Phys.* **2012**, *14*, 16192−16196.

(56) Brus, L. E. Electronic Wave Functions in Semiconductor Clusters: Experiment and Theory. *J. Phys. Chem.* **1986**, *90*, 2555−2560.

(57) Wang, Y.; Suna, A.; Mahler, W.; Kasowski, R. PbS in Polymers. From Molecules to Bulk Solids. *J. Chem. Phys.* **1987**, *87*, 7315−7322.

(58) Chen, B.; Uher, C.; Iordanidis, L.; Kanatzidis, M. G. Transport Properties of Bi_2S_3 and the Ternary Bismuth Sulfides $KBi_{6.33}S_{10}$ and $K_2Bi_8S_{13}$. *Chem. Mater.* **1997**, *9*, 1655−1658.

(59) Jun, H. K.; Careem, M. A.; Arof, A. K. Quantum Dot-Sensitized Solar Cells—Perspective and Recent Developments: A Review of Cd Chalcogenide Quantum Dots as Sensitizers. *Renewable Sustainable Energy Rev.* **2013**, *22*, 148−167.

(60) Mikla, V. I.; Mikla, V. V. *Metastable States in Amorphous Chalcogenide Semiconductors*; Springer Series in Materials Science 128; Springer: Berlin, Germany, 2010.

11504

dx.doi.org/10.1021/jp411516a | *J. Phys. Chem. C* 2014, 118, 11495−11504